Applied Physics Letters ARTICLE scitation.org/journal/apl

High-performance germanium quantum dot photodetectors: Response to continuous wave and pulsed excitation

Cite as: Appl. Phys. Lett. **117**, 251105 (2020); doi: 10.1063/5.0025660
Submitted: 18 August 2020 · Accepted: 10 December 2020 ·
Published Online: 22 December 2020

S. Shi,[1,a)] A. Zaslavsky,[1,2] and D. Pacifici[1,2]

AFFILIATIONS

[1]School of Engineering, Brown University, Providence, Rhode Island 02912, USA
[2]Department of Physics, Brown University, Providence, Rhode Island 02912, USA

[a)]Author to whom correspondence should be addressed: sue_shi@brown.edu

ABSTRACT

Efficiency and response speed are key figures of merit for high-performance photodetectors, with high efficiency often obtained at the expense of slow photoresponse. Here, we report on germanium quantum dot photodetectors (Ge QD PDs) with a 25-nm-thick active layer that possesses both high internal quantum efficiency (IQE) and fast photoresponse, yet is still based on simple design and fabrication. We characterize these devices with continuous wave (CW) and pulsed excitation at room temperature as a function of incident power and applied bias. Under the reverse bias of −4 V, the IQE approaches ∼2000% over a broad spectral range ($\lambda = 500$–800 nm). The transient photoresponse speed to a 4.5 ns laser pulse at $\lambda = 640$ nm is under 20 ns. Furthermore, we observe an interesting phenomenon: by superimposing a weak CW HeNe laser beam ($\lambda = 632.8$ nm) on the laser pulse, we obtain an optically tunable photoresponse while retaining fast speed. This study elucidates the role of photocarrier generation, trapping, and hopping in the percolative Ge QD oxide matrix and helps explain the observed high gain and fast response speed. The demonstrated IQE and nanosecond response time render our devices suitable for low-light detection and imaging.

Quantum dots are attractive for applications in optoelectronic devices, including photodetectors,[1–3] light emitting diodes,[4] lasers,[5–7] and phototransistors,[8] thanks to their spectral tunability. In particular, silicon (Si) and germanium (Ge) QDs are of great interest due to their potential compatibility with Si technology.[9–14] Germanium offers some advantages over Si for use in QD devices, including a lower synthesis temperature[15,16] and a larger excitonic Bohr radius, which enables stronger quantum confinement.[17] Germanium QDs embedded in an oxide matrix have been studied extensively,[18–23] and photodetectors based on Ge QDs have achieved up to 1500% IQE,[24] as well as broad spectral coverage from near-ultraviolet to near-infrared wavelengths.[20,25]

However, a trade-off between quantum efficiency and response speed has often been reported,[26–28] and overcoming it is key to improving overall PD performance. Another crucial factor is the fabrication simplicity. A number of recently reported photodetectors[8,29,30] with excellent sensitivity require fairly complex structures and fabrication techniques. Our simple design (see Fig. 1) and fabrication method yield high-performance devices without sacrificing easy integration.

In this Letter, we report on a Ge QD PD with a thin active layer of 25 nm, which has a high IQE exceeding 2000% at 640 nm, in addition to response times down to ∼10 ns. We are able to obtain both high efficiency and fast response speed by thinning the active layer and taking advantage of the hole-trapping conduction mechanism that provides internal gain in these devices.[31] We present a detailed study on the photoresponse of Ge QD PDs to both CW and ultrashort pulsed excitation, as a function of applied bias and incident power. We also investigate the effect of an external resistor R_{ext} on the transient photoresponse. Finally, we demonstrate a two-beam characterization scheme, where the transient photoresponse of the Ge QD PD to an ultrashort laser pulse can be controlled with a much weaker CW beam. These experiments support the hypothesis of QD-assisted charge trapping and percolation as physical processes likely responsible for the observed high quantum efficiency and fast photoresponse.

Amorphous Ge and SiO_2 were simultaneously sputtered from two different targets onto a heated n-Si substrate held at 400 °C using an Angstrom AMOD Physical Vapor Deposition Platform. The deposited film was subsequently annealed at 500 °C in an N_2 atmosphere for 30 min to generate densely packed Ge QDs with higher crystalline quality.[32] The final thickness of the annealed film consisting of Ge QDs embedded in the SiO_2 matrix is ∼25 nm, measured by

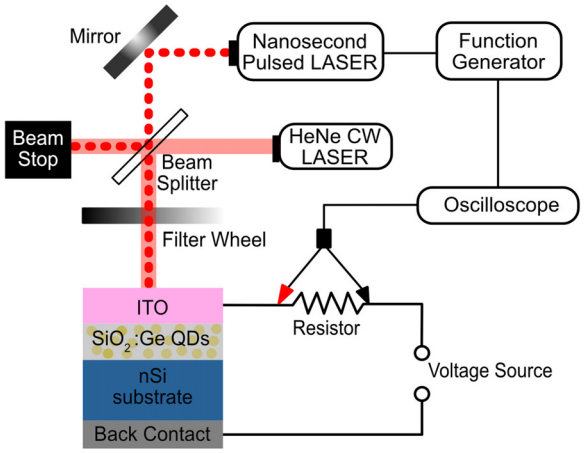

FIG. 1. Schematic of the experimental setup for Ge QD PD transient response characterization. The HeNe CW laser was only turned on during the two-beam experiment; the device active area was $2 \times 2\,\text{mm}^2$.

variable angle spectroscopic ellipsometry (VASE, Woollam M-2000). An ~70-nm-thick indium tin oxide (ITO) layer was sputtered at room temperature with 10% O_2 flow and 60 W DC power onto lithographically defined 4 mm^2 active areas. After lift-off, annealing at 400 °C in N_2 for 30 minutes determined an ITO sheet resistance of ~160 Ω/□.

Current–voltage (I–V) characterization under CW excitation was performed using a QEX10 quantum efficiency measurement system (PV Measurements, Inc.). Specular reflectance was measured after calibration with a single-polished 1-cm-thick Si substrate over the $\lambda = 400$–1100 nm range. The transient photoresponse of the Ge QD PDs was probed with a $\lambda = 640$ nm Nanosecond Pulsed Laser Diode System (Thorlabs, Inc.) set to the shortest 4.5 ns pulse width and triggered by a 1 kHz square wave. A schematic of the experimental setup is shown in Fig. 1, with the CW HeNe laser (Thorlabs, Inc.) at $\lambda = 632.8$ nm only used for two-beam characterization. The beam splitter ensured an identical optical path for both laser beams. The neutral density filter wheel enabled power dependence characterization. The signal was read out from a series resistor R_{ext} using an oscilloscope. All measurements were performed with $R_{ext} = 100\ \Omega$ unless otherwise noted.

The I–V characteristics of the Ge QD PD shown in Fig. 2(a) were investigated as a function of applied bias under $\lambda = 640$ nm CW excitation for various incident powers P_{in}. At a given P_{in}, the current first increases rapidly with increasing reverse bias and then saturates, with the saturation occurring at a higher reverse bias for higher P_{in}. Similarly, at a given reverse bias, the current increases rapidly with P_{in} and then tends to saturate.

Figure 2(b) shows the spectral responsivity (R_{sp}, left axis) and the corresponding IQE (defined as the ratio between the number of collected charge carriers and the number of absorbed photons, right axis) as a function of incident power for various reverse bias values, derived from Fig. 2(a) using the following equations:

$$R_{sp}(\lambda) = \frac{I_{ph}(\lambda)}{P_{in}} = \frac{I_{light}(\lambda) - I_{dark}}{P_{in}}, \tag{1}$$

$$\text{IQE}(\lambda) = \frac{hc}{\lambda q(1 - R(\lambda))} R_{sp}(\lambda), \tag{2}$$

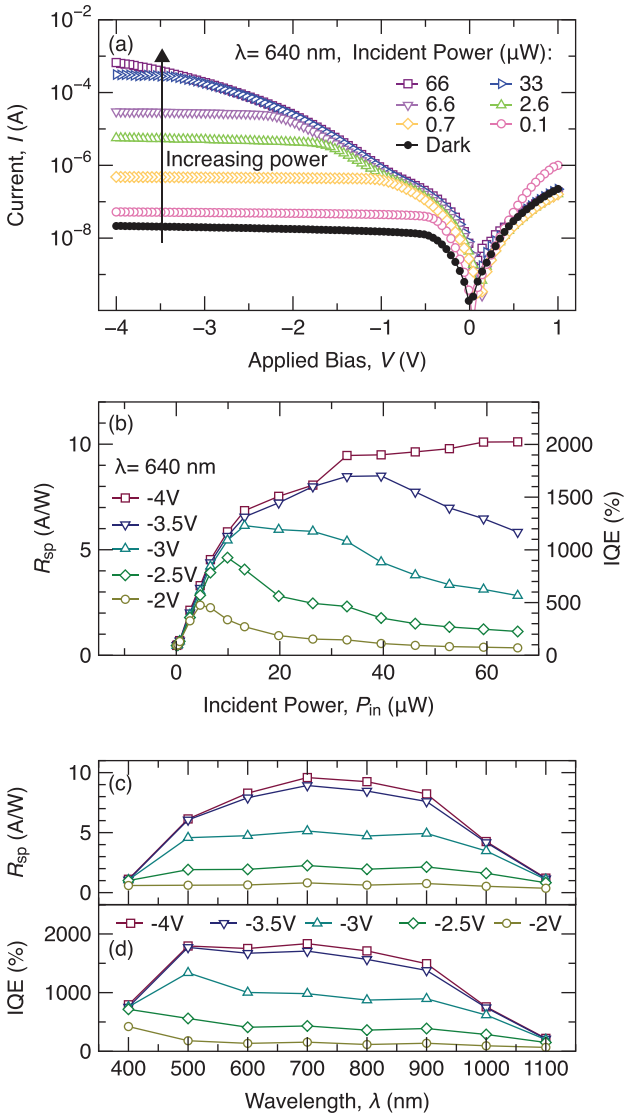

FIG. 2. (a) I–V curves of the Ge QD PD when exposed to $\lambda = 640$ nm CW excitation for a range of incident powers. (b) The corresponding R_{sp} (left axis) and IQE (right axis) derived from (a), plotted as a function of P_{in} for various reverse bias values. (c) R_{sp} and (d) IQE vs wavelength for various reverse bias values at $P_{in} = 33\ \mu$W.

where I_{ph} is the photocurrent, defined as the difference between the total current under illumination (I_{light}) and the dark current (I_{dark}); P_{in} is the power incident on the PD active area; h is Planck's constant; c is the speed of light; λ is the excitation wavelength; q is the electron charge; R is the specular reflectance. The maximum R_{sp} (and, correspondingly, IQE) represented by the peak of each curve in Fig. 2(b) shifts toward lower incident power with decreasing reverse bias. This trend implies a percolative conduction mechanism through the Ge QD layer: reduced reverse bias decreases the energy range of percolation pathways through the QD-containing active layer, thereby limiting carrier transport across the device and causing response saturation. The percolation model has been proposed for charge transport through other types of QD networks.[33–35]

Figure 2(c) shows R_{sp} and Fig. 2(d) shows the IQE, both as a function of λ at CW $P_{in} = 33\ \mu$W. The device maintains high R_{sp} and IQE across the entire measured visible spectrum and up to at least $\lambda = 1000$ nm in the near-IR. Since most of the absorption takes place in the substrate, the IQE is reduced when the incident wavelengths exceed the absorption limit of silicon.[25]

The high IQE obtained is attributed to dynamical hole trapping in these devices:[24,25] holes trapped in QDs induce electron injection from the ITO top contact to maintain charge neutrality within the device. This mechanism should not be significantly affected by the thickness of the active layer, and so reducing it helps improve the speed without impacting the responsivity, provided that the active layer is thick enough to prevent a high unwanted I_{dark} due to direct tunneling. In fact, with a 25 nm active layer, the reported device has higher R_{sp} and IQE than devices with thicker 60–110 nm active layers.

Transient photoresponse curves to a 4.5 ns laser pulse at $\lambda = 640$ nm and $P_{in} = 120$ mW are shown in Fig. 3(a) for several reverse bias values. Each transient curve consists of a sharp first peak followed by a broader second peak due to circuit ringing, a phenomenon further examined in Fig. 4. To calculate the IQE of the pulsed response, we take the ratio between the number of collected carriers and the number of absorbed photons. We integrate the photocurrents in Fig. 3(a) to obtain the total number of carriers collected and integrate the laser pulse to obtain the total pulse energy, which can be converted to total photons absorbed by taking into account the reflectance at $\lambda = 640$ nm (~3%). Figure 3(b) shows that the IQE from pulsed excitation tends to saturate around 300% under the applied bias of –2 V, confirming low-voltage operation capability. Compared to IQE

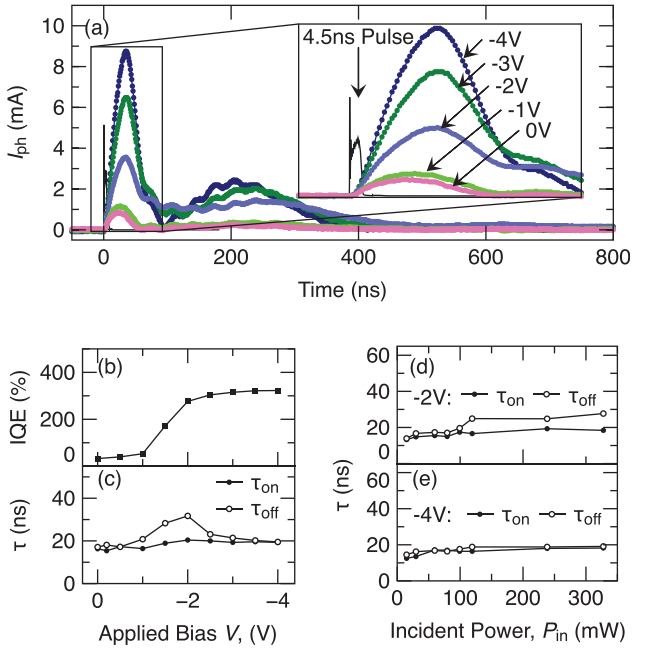

FIG. 3. (a) Transient response to a 4.5 ns pulse at $\lambda = 640$ nm under various applied bias values at a fixed $P_{in} = 120$ mW. The photoresponse consists of a sharp first peak and a broader second peak. (b) IQE and (c) rise and fall times of the first peak (τ_{on} and τ_{off}) vs applied bias at $P_{in} = 120$ mW. τ_{on} and τ_{off} vs P_{in}, at (d) –2 and (e) –4 V applied bias.

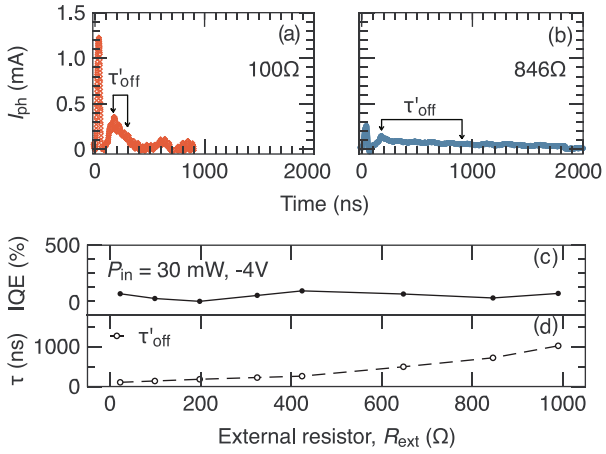

FIG. 4. Transient response at $P_{in} = 30$ mW under the reserve bias of –4 V with $R_{ext} =$ (a) 100 Ω and (b) 846 Ω. (c) IQE and (d) second peak fall time (τ'_{off}) vs R_{ext}.

values under CW excitation and the same reverse bias, the pulse response IQEs are lower, while the average pulse power is much higher than that under CW excitation. As the high-power pulsed excitation generates a high density of carriers in the substrate near the QD-containing active layer, a reverse bias up to –4 V is not sufficient to allow tunneling and transport of all the pulse-generated carriers through all the existing percolation pathways. This causes higher carrier recombination in the substrate and lower collection efficiency. The IQE is, therefore, lower under pulsed excitation compared to the CW–IQE results reported in Fig. 2, but still exceeds 100% beyond the reverse bias of –1.5 V. The rise (τ_{on}) and fall (τ_{off}) times in Fig. 3(c) are extracted from the first peak of the transient photoresponse curves in Fig. 3(a), defined as the time taken to rise to 1–1/e and fall to 1/e of the peak value, respectively. Both τ_{on} and τ_{off} remain below 35 ns over the entire reverse bias range and for all values of P_{in} at reverse bias values of –2 and –4 V, as shown in Figs. 3(c)–3(e). We find that τ_{on} and τ_{off} are relatively constant over the measured power range, with no appreciable difference between reverse bias values of –2 and –4 V. This reaffirms that our PDs can be operated at a low voltage of –2 V and achieve high performance.

We varied R_{ext} to investigate its effect on the circuit. Figures 4(a) and 4(b) show the pulsed response of our PD with $R_{ext} = 100$ and 846 Ω, respectively, at $P_{in} = 30$ mW and the reverse bias of –4 V. Since P_{in} and applied bias are fixed, the total charge collected should not vary significantly with R_{ext}, as evidenced by the IQE, which is directly proportional to the total collected charge, plotted as a function of R_{ext} in Fig. 4(c). While the total charge is unaffected by R_{ext}, the charge distribution varies with R_{ext}, as higher R_{ext} values result in slower circuit ringing effects. This difference in charge distribution causes the second peak in the transient photoresponse to yield varying fall times τ'_{off} [defined as the time it takes for the second peak to fall to 1/e of its value, see arrows in Figs. 4(a) and (b)], which increases rapidly with higher R_{ext}, as shown in Fig. 4(d).

Turning on both the CW HeNe and the pulsed laser (setup shown in Fig. 1) yields an interesting phenomenon. At low reverse bias values, the addition of a much weaker CW excitation strongly

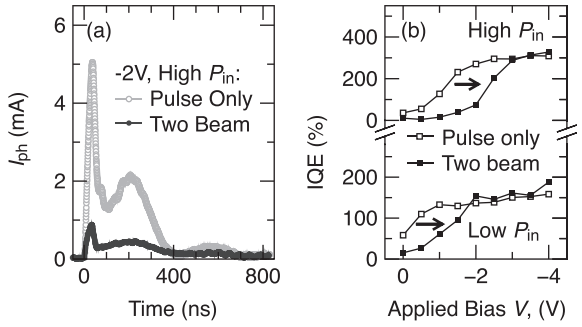

FIG. 5. (a) Transient response at pulsed $P_{in} = 120$ mW with (black circles) and without (grey circles) a 30 μW HeNe CW laser, measured under the reverse bias of –2 V. (b) IQE vs applied bias for high pulsed $P_{in} = 120$ mW with CW $P_{in} = 30$ μW (labeled high P_{in}) and low pulsed $P_{in} = 30$ mW with CW $P_{in} = 7.5$ μW (labeled low P_{in}).

suppresses the pulse-generated photocurrent, as shown in Fig. 5(a) for the reverse bias of –2 V. The carriers generated by the ~3 orders of magnitude lower-power CW laser cause a saturation of the percolation paths that are no longer available when the pulsed laser is turned on, which causes a remarkable reduction in the carrier collection efficiency and hence photocurrent, once the laser pulse is turned on. To further validate this hypothesis, we compared the measured IQEs between under pulse-only and two-beam excitation conditions, both as a function of applied bias, as shown in Fig. 5(b) for pulsed $P_{in} = 120$ mW and 30 mW. Both IQE curves resemble the shape of the pulsed response IQE curve in Fig. 3(b), but the weak CW beam shifts the rise in the pulsed IQE curve toward higher reverse bias. This rightward shift suggests that the presence of a CW background requires higher reverse bias to reach the same internal quantum efficiency, implying that more percolation pathways have to be established to efficiently transport the extra CW-generated carriers. For high $P_{in} = 120$ mW, the suppression persists until –3.5 V, whereas for low $P_{in} = 30$ mW, the crossover point occurs at the reverse bias around –2 V. While a full model of optical control of the pulsed photoresponse remains to be developed, the possibility of tuning pulsed PD performance optically may find useful applications.

In summary, we demonstrate highly efficient and fast Ge QD PDs with a thin active layer (25 nm) that allows for fast charging and discharging dynamics and high IQE due to hole-assisted charge trapping and percolation. Under $\lambda = 640$ nm CW excitation, the IQE of the device surpasses 2000% under the applied bias of –4 V and remains above 700% across the visible spectrum. The response speed to a 4.5 ns pulsed laser reaches down to ~10 ns for τ_{on} and ~20 ns for τ_{off}. R_{ext} is shown to only affect circuit ringing, while the response times (both τ_{on} and τ_{off}) from the first peak of the transient photoresponse curve remain unaffected across the measured range of applied bias and incident power. Two-beam characterization shows that the addition of a weak CW excitation can be used to suppress the transient response to pulsed excitation, a phenomenon attributable to the occupation of available percolation pathways by the CW-induced carriers. The reported high efficiency and fast response speed show promise for compact, high-performance, broadband imaging cameras based on germanium quantum dot photodetectors. The ability to control the transient photoresponse using a weak CW signal offers potential for optically controlled PDs based on this device structure.

The work on Ge QD PDs at Brown was originally funded by NSF Award No. DMR-1203186; we also acknowledge the maskless lithography tool funded by the No. DMR-1827453 MRI award. Finally, the authors gratefully acknowledge D. C. Paine, H. Wang, R. Zia, and J. D. L. Ferro for valuable discussions and technical support.

DATA AVAILABILITY

The data that support the findings of this study are available from the corresponding author upon reasonable request.

REFERENCES

[1]H. C. Liu, M. Gao, J. McCaffrey, Z. Wasilewski, and S. Fafard, "Quantum dot infrared photodetectors," Appl. Phys. Lett. **78**, 79–81 (2001).
[2]J. P. Clifford, G. Konstantatos, K. W. Johnston, S. Hoogland, L. Levina, and E. H. Sargent, "Fast, sensitive and spectrally tuneable colloidal-quantum-dot photodetectors," Nat. Nanotechnol. **4**, 40–44 (2009).
[3]A. V. Barve, S. J. Lee, S. K. Noh, and S. Krishna, "Review of current progress in quantum dot infrared photodetectors," Laser Photonics Rev. **4**, 738–750 (2010).
[4]V. Wood and V. Bulović, "Colloidal quantum dot light-emitting devices," Nano Rev. **1**, 5202 (2010).
[5]M. Grundmann, "The present status of quantum dot lasers," Physica E **5**, 167–184 (1999).
[6]N. N. Ledentsov, "Quantum dot laser," Semicond. Sci. Technol. **26**, 014001 (2011).
[7]M. Grydlik, F. Hackl, H. Groiss, M. Glaser, A. Halilovic, T. Fromherz, W. Jantsch, F. Scha.ffler, and M. Brehm, "Lasing from glassy Ge quantum dots in crystalline Si," ACS Photonics **3**, 298–303 (2016).
[8]M.-H. Kuo, M.-C. Lee, H.-C. Lin, T. George, and P.-W. Li, "High photoresponsivity Ge-dot photoMOSFETs for low-power monolithically-integrated Si optical interconnects," Sci. Rep. **7**, 44402 (2017).
[9]K. L. Wang, D. Cha, J. Liu, and C. Chen, "Ge/Si self-assembled quantum dots and their optoelectronic device applications," Proc. IEEE **95**, 1866–1883 (2007).
[10]E. G. Barbagiovanni, D. J. Lockwood, P. J. Simpson, and L. V. Goncharova, "Quantum confinement in Si and Ge nanostructures: Theory and experiment," Appl. Phys. Rev. **1**, 011302 (2014).
[11]A.-M. Lepadatu, A. Slav, C. Palade, I. Dascalescu, M. Enculescu, S. Iftimie, S. Lazanu, V. Teodorescu, M. Ciurea, and T. Stoica, "Dense Ge nanocrystals embedded in TiO_2 with exponentially increased photoconduction by field effect," Sci. Rep. **8**, 4898 (2018).
[12]Z. Ni, S. Zhou, S. Zhao, W. Peng, D. Yang, and X. Pi, "Silicon nanocrystals: Unfading silicon materials for optoelectronics," Mater. Sci. Eng., R **138**, 85–117 (2019).
[13]I. Stavarache, V. A. Maraloiu, C. Negrila, P. Prepelita, I. Gruia, and G. Iordache, "Photo–sensitive Ge nanocrystal based films controlled by substrate deposition temperature," Semicond. Sci. Technol. **32**, 105003 (2017).
[14]I. Stavarache, C. Logofatu, M. T. Sultan, A. Manolescu, H. G. Svavarsson, V. S. Teodorescu, and M. L. Ciurea, "SiGe nanocrystals in SiO_2 with high photosensitivity from visible to short–wave infrared," Sci. Rep. **10**, 3252 (2020).
[15]B. Zhang, S. Shrestha, M. Green, and G. Conibeer, "Size controlled synthesis of Ge nanocrystals in SiO_2 at temperatures below 400 C using magnetron sputtering," Appl. Phys. Lett. **96**, 261901 (2010).
[16]D. Pacifici, E. Moreira, G. Franzò, V. Martorino, F. Priolo, and F. Iacona, "Defect production and annealing in ion-irradiated Si nanocrystals," Phys. Rev. B **65**, 144109 (2002).
[17]Y. Maeda, "Visible photoluminescence from nanocrystallite Ge embedded in a glassy SiO_2 matrix: Evidence in support of the quantum–confinement mechanism," Phys. Rev. B **51**, 1658 (1995).

[18]B.-C. Hsu, S. Chang, T.-C. Chen, P.-S. Kuo, P. Chen, Z. Pei, and C. Liu, "A high efficient 820 nm MOS Ge quantum dot photodetector," IEEE Electron Device Lett. **24**, 318–320 (2003).
[19]S. Tzeng and P.-W. Li, "Enhanced 400–600 nm photoresponsivity of metal–oxide–semiconductor diodes with multi–stack germanium quantum dots," Nanotechnology **19**, 235203 (2008).
[20]C. Chien, W. Lai, Y. Chang, C. Wang, M. Kuo, and P.-W. Li, "Size tunable Ge quantum dots for near–ultraviolet to near–infrared photosensing with high figures of merit," Nanoscale **6**, 5303–5308 (2014).
[21]D. Lehninger, J. Beyer, and J. Heitmann, "A review on Ge nanocrystals embedded in SiO_2 and high-k dielectrics," Phys. Status Solidi A **215**, 1701028 (2018).
[22]I. Stavarache, V. S. Teodorescu, P. Prepelita, C. Logofatu, and M. L. Ciurea, "Ge nanoparticles in SiO_2 for near infrared photodetectors with high performance," Sci. Rep. **9**, 10286 (2019).
[23]V. Dhyani, G. Ahmad, N. Kumar, and S. Das, "Size–dependent photoresponse of Ge nanocrystals–metal oxide semiconductor photodetector," IEEE Trans. Electron Devices **67**, 558–565 (2020).
[24]S. Cosentino, E. Barbagiovanni, I. Crupi, M. Miritello, G. Nicotra, C. Spinella, D. Pacifici, S. Mirabella, and A. Terrasi, "Size dependent light absorption modulation and enhanced carrier transport in germanium quantum dots devices," Sol. Energy Mater. Sol. Cells **135**, 22–28 (2015).
[25]S. Siontas, H. Wang, D. Li, A. Zaslavsky, and D. Pacifici, "Broadband visible–to–telecom wavelength germanium quantum dot photodetectors," Appl. Phys. Lett. **113**, 181101 (2018).
[26]J. Bowers and C. Burrus, "Ultrawide-band long-wavelength pin photodetectors," J. Lightwave Technol. **5**, 1339–1350 (1987).
[27]J. B. Soole and H. Schumacher, "InGaAs metal-semiconductor-metal photodetectors for long wavelength optical communications," IEEE J. Quantum Electron. **27**, 737–752 (1991).
[28]R. Ghayour and A. Bakhtazad, "Trade-off between speed and efficiency of silicon metal–i–n photodetectors," Solid-State Electron. **42**, 715–720 (1998).
[29]N. J. Martinez, C. T. Derose, R. W. Brock, A. L. Starbuck, A. T. Pomerene, A. L. Lentine, D. C. Trotter, and P. S. Davids, "High performance waveguide-coupled Ge-on-Si linear mode avalanche photodiodes," Opt. Express **24**, 19072–19081 (2016).
[30]M. Takiguchi, N. Takemura, K. Tateno, K. Nozaki, S. Sasaki, S. Sergent, E. Kuramochi, T. Wasawo, A. Yokoo, A. Shinya *et al.*, "All-optical InAsP/InP nanowire switches integrated in a Si photonic crystal," ACS Photonics **7**, 1016–1021 (2020).
[31]S. Cosentino, S. Mirabella, P. Liu, S. T. Le, M. Miritello, S. Lee, I. Crupi, G. Nicotra, C. Spinella, D. Paine, A. Terrasi, A. Zaslavsky, and D. Pacifici, "Role of Ge nanoclusters in the performance of photodetectors compatible with Si technology," Thin Solid Films **548**, 551–555 (2013).
[32]S. Cosentino, S. Mirabella, M. Miritello, G. Nicotra, R. L. Savio, F. Simone, C. Spinella, and A. Terrasi, "The role of the surfaces in the photon absorption in Ge nanoclusters embedded in silica," Nanoscale Res. Lett. **6**, 135 (2011).
[33]Y. Zhang, D. Zherebetskyy, N. D. Bronstein, S. Barja, L. Lichtenstein, D. Schuppisser, L.-W. Wang, A. P. Alivisatos, and M. Salmeron, "Charge percolation pathways guided by defects in quantum dot solids," Nano Lett. **15**, 3249–3253 (2015).
[34]J. Laube, S. Gutsch, D. Wang, C. Kübel, M. Zacharias, and D. Hiller, "Two-dimensional percolation threshold in confined Si nanoparticle networks," Appl. Phys. Lett. **108**, 043106 (2016).
[35]Y. Zhang, D. J. Hellebusch, N. D. Bronstein, C. Ko, D. F. Ogletree, M. Salmeron, and A. P. Alivisatos, "Ultrasensitive photodetectors exploiting electrostatic trapping and percolation transport," Nat. Commun. **7**, 11924 (2016).